RESEARCH ARTICLE

α-*N*-Methyltransferase regiospecificity is mediated by proximal, redundant enzyme–substrate interactions

Kathryn K. Crone[1] ⓘ | Jason W. Labonte[2] | Mikael H. Elias[1,3] ⓘ | Michael F. Freeman[1,3] ⓘ

[1]Department of Biochemistry, Molecular Biology, and Biophysics, University of Minnesota Twin Cities, St. Paul, Minnesota, USA

[2]Department of Chemistry, Notre Dame of Maryland University, Baltimore, Maryland, USA

[3]Department of Biochemistry, Molecular Biology, and Biophysics and BioTechnology Institute, University of Minnesota Twin Cities, St. Paul, Minnesota, USA

Correspondence
Michael F. Freeman and Mikael H. Elias, Department of Biochemistry, Molecular Biology, and Biophysics and BioTechnology Institute, University of Minnesota Twin Cities, St. Paul, MN 55108, USA.
Email: mffreema@umn.edu and mhelias@umn.edu

Review Editor: Aitziber L. Cortajarena

Abstract

N-Methylation of the peptide backbone confers pharmacologically beneficial characteristics to peptides that include greater membrane permeability and resistance to proteolytic degradation. The borosin family of ribosomally synthesized and post-translationally modified peptides offer a post-translational route to install amide backbone α-*N*-methylations. Previous work has elucidated the substrate scope and engineering potential of two examples of type I borosins, which feature autocatalytic precursors that encode *N*-methyltransferases that methylate their own C-termini in trans. We recently reported the first discrete *N*-methyltransferase and precursor peptide from *Shewanella oneidensis* MR-1, a minimally iterative, type IV borosin that allowed the first detailed kinetic analyses of borosin *N*-methyltransferases. Herein, we characterize the substrate scope and resilient regiospecificity of this discrete *N*-methyltransferase by comparison of relative rates and methylation patterns of over 40 precursor peptide variants along with structure analyses of nine enzyme–substrate complexes. Sequences critical to methylation are identified and demonstrated in assaying minimal peptide substrates and non-native peptide sequences for assessment of secondary structure requirements and engineering potential. This work grants understanding towards the mechanism of substrate recognition and iterative activity by discrete borosin *N*-methyltransferases.

KEYWORDS
amide *N*-methylation, biocatalysis, borosin, *N*-methyltransferase, RiPP

1 | INTRODUCTION

N-Methylation of the peptide backbone can often enhance peptide bioavailability, structural rigidity, and stability. The substitution with the methyl group disables

hydrogen-bond donation by the backbone amide nitrogen, decreasing the hydrophilicity of the molecule. The loss of hydrogen-bonding donors also affects peptide secondary structure and the probability of the backbone to occupy certain conformations (Chatterjee et al. 2013).

Many applications for cyclic and linear *N*-methylated peptides exist in clinical settings, including the well-known immunosuppressant cyclosporin A (Borel and Feurer 1977). More recently, linear *N*-methylated peptides have shown potential to cap β-sheets associated with amyloid plaques (Sciarretta et al. 2006; Soto et al. 2007).

Although the pharmacologic benefits of peptide *N*-methylation have been recognized for decades, the routes for synthesizing *N*-methylated peptides are limited, making it a challenge to apply peptide *N*-methylation to broader drug screening efforts. Most common, traditional synthetic methods are intensive and often not modular (Chatterjee et al. 2012; Li et al. 2023). In addition, many of the cyclic *N*-methylated peptides originally isolated from natural sources, like cyclosporin A, are of non-ribosomal origin. Non-ribosomal peptide synthetases are large multi-domain protein complexes, the production of which—despite some progress—is not easily scaled up or diversified (Cai et al. 2023; Zhang et al. 2023). Alternatively, *N*-methyl amino acids can be incorporated into growing peptides by the ribosome using cell-free translation approaches. However, these routes have drawbacks, which include low product yields and limited codon usage, reducing the variety and number of *N*-methyl amino acids that can be incorporated by the ribosome without significant additional engineering efforts (Iwane et al. 2021; Kawakami et al. 2008; Subtelny et al. 2008). In the above biosynthetic examples, the *N*-methyl group is installed on the primary amine before the amide bond is formed. Within the past several years, however, *N*-methylation has been discovered as a post-translational modification in the family of ribosomally synthesized and post-translationally modified peptides (RiPPs) called borosins (Ramm et al. 2017; van der Velden et al. 2017).

RiPPs are a large class of peptide natural products featuring a wide variety of both peptide backbone and side-chain modifications (Arnison et al. 2013; Montalbán-López et al. 2021). RiPPs provide compact and modular biosynthetic routes for the production of highly modified peptides that can have applications in biotechnology and peptide drug design. In microbes, RiPP pathways are often encoded in monocistronic gene clusters less than 20 kilobases in length. The amino acid sequence for the final natural product is encoded in a precursor peptide that is typically composed of two regions, an N-terminal leader peptide and a C-terminal core peptide. After transcription and translation of the precursor sequence, the leader is recognized by tailoring enzymes that post-translationally modify the core peptide. A final protease-mediated maturation step is often needed to release the final natural product for export out of the host cell (Arnison et al. 2013; Montalbán-López et al. 2021). In many RiPP families, the relay of specific interactions for modifying enzymes to the leader peptide results in enhanced core-peptide sequence plasticity that affords the production of a variety of modified peptides (Deane et al. 2016; DiCaprio et al. 2019; Himes et al. 2016; Li et al. 2010). However, other RiPP systems require additional N- or C-terminal recognition sequences for post-translational modifications of core peptides (Goto et al. 2014; Sardar et al. 2015b; Song et al. 2021b). Thus, a mechanistic understanding of how tailoring enzymes bind and site-specifically modify a substrate is a necessity to effectively use RiPPs in biotechnological applications, including peptide drug biosynthesis.

Borosin methyltransferases compose a large enzyme family capable of post-translationally installing *N*-methyl groups on the backbone amide groups of peptides. While this biosynthetic strategy was initially discovered and characterized in fungi, recent bioinformatics analyses have uncovered more than 2500 borosin gene clusters present in all domains of life (Lee et al. 2024). Borosin methyltransferases and precursor peptides have been organized into 11 structural types, based on a combination of unique protein-domain organization and distinct properties of the core peptides (Imani et al. 2022; Lee et al. 2024; Quijano et al. 2019). Initial efforts have been made with the family's founding type I member, OphMA, to determine the substrate scope for the methylation reaction (Song et al. 2020). In addition, OphMA and related MroMA1 were subjected to protein-engineering efforts (Song et al. 2021a; Zheng et al. 2022). However, these type I borosin methyltransferases compose one of only two RiPP families that feature a modification enzyme fused to their core peptides (Kersten et al. 2022; Mydy et al. 2024). Despite initial progress, the fused enzyme–substrate architecture of type I borosins limit their utility in the biotechnological production of diverse *N*-methylated peptides.

In contrast, the type IV "split borosins," hallmarked by the pathway from *Shewanella oneidensis* MR-1 producing shewanellamide A (Crone et al. 2023; Miller et al. 2021), provide a more amenable protein architecture for *N*-methylated peptide production (Figure 1). Here the *N*-methyltransferase (SonM) and precursor peptide (SonA) are encoded discretely, allowing for multiple substrate turnovers when the methyl donor—*S*-adenosyl-L-methionine (SAM)—and *S*-adenosylhomocysteine nucleosidase (SAHN) are included in the reaction. With only two methylations, on L63 and I65 of the core peptide, this minimally iterative system served well for the first in-depth kinetic analysis of peptide substrates for *N*-methylation. Measured reaction rates via a coupled-enzyme kinetics assay have shown apparent k_{cat} and K_M values of 0.52 min^{-1} and 8 μM, respectively (Miller
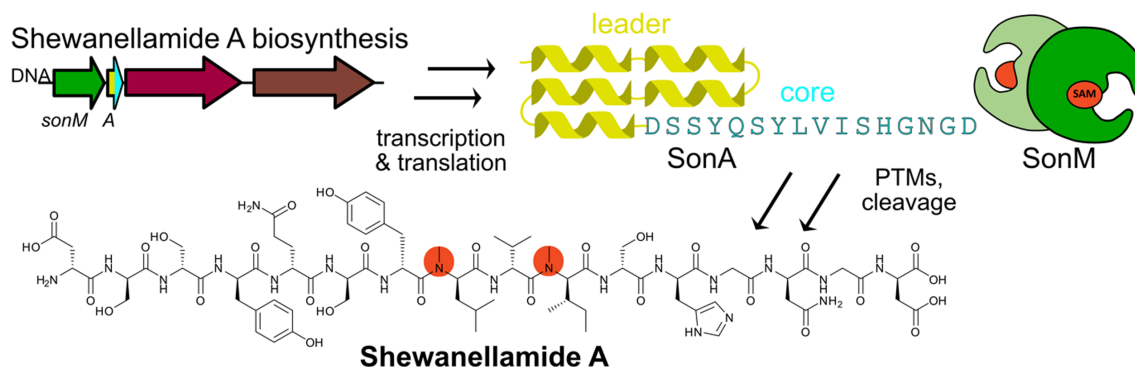
FIGURE 1　Biosynthesis of the RiPP natural product shewanellamide A. The biosynthetic gene cluster is depicted by colored arrows. After transcription and translation, SonA is methylated by SonM. Proteolysis then releases the mature shewanellamide A peptide.

et al. 2021). This marked SonM as the fastest borosin methyltransferase characterized thus far, where OphMA is considerably slower (in vitro $k_{cat,App}$ of 0.12 h^{-1}) (Song et al. 2018). Previously, relying on kinetic modeling data, we predicted the mono-N-methylated SonA peptide is able to dissociate from SonM, and both methylation events have near equivalent catalytic efficiencies (Miller et al. 2021).

The N-terminal leader peptide of SonA is composed of a five-helix bundle (SonA 1–55), termed the borosin-binding domain (BBD). Depending on the methylation state of the core peptide, our previous structural data models the fifth helix of the BBD either wound or unwound when associated with SonM, revealing metamorphic properties of the SonA leader peptide (Miller et al. 2021). Concomitantly, the core peptide also displays metamorphic characteristics. While the fully methylated SonA core is modeled as a structured coil, the unmethylated core (SonA 56–71) was modeled as an α-helix in the SonM active site. These large structural differences sparked the hypothesis that SonA secondary structural changes induced by backbone methylation may drive the iterative activity of SonM (Miller et al. 2021). More recent work delving into the boundaries of the SonA precursor peptide revealed that SonM activity and regiospecificity is maintained in the complete absence of the fifth "metamorphic" helix of the BBD. A change in the methylation pattern could only be achieved upon deletion of Q60–Y62 in SonA, which is immediately N-terminal to the first methylation site at L63 (Crone et al. 2023). Thus, further understanding of how regiospecificity is determined in borosin natural product biosynthesis would guide future engineering efforts to enable the creation of custom backbone N-methylated peptides.

Here, we present an extensive analysis of substrate structure–activity relationships of SonM and SonA in our model borosin pathway. We use a combination of comparative reaction rates, relative methylation abundance,

and multiple X-ray crystal structures to probe SonM substrate scope at the positions of methylation. We further assess contributions to regiospecificity and iterative activity from regions N- and C-terminal to methylation using a combination of alanine scanned and truncated SonA variants. We also show that the BBD and core peptide can work in trans, where nominal methylation can occur on the core peptide even in the absence of the BBD. To address our previous hypothesis of changes in the helical core driving iterative methylation, we wrote an in-house script to scrape sequences from the PDB with defined secondary structures to assay whether SonM can methylate similar sequences with presumably different secondary structures. Utilizing this collective set of information, we engineered core peptides to accommodate up to four backbone methylations with an enzyme that is otherwise recalcitrant to changes in regiospecificity.

2 | RESULTS AND DISCUSSION

2.1 | SonA L63 and I65 variant effects on regiospecificity and iterative activity

Previous crystal structures have shown minimal evidence towards the importance of side chain interactions at the site of methylation (i) or the binding pockets preceding $(i - n)$ or following $(i + n)$ modification (Miller et al. 2021). To test the substrate scope of SonM, a set of SonA point variants at the L63 and I65 position were constructed. Amino acid residues with a variety of properties, including size, polarity, and charge, were chosen to gauge their effect on substrate turnover and regiospecificity. Variants were then assayed with wildtype (wt) SonM in vitro, and reaction rates were measured via our previously optimized coupled-enzyme kinetics assay (Figure 2a) (Miller et al. 2021). In parallel, methylation patterns were analyzed after 16-h overnight reactions by
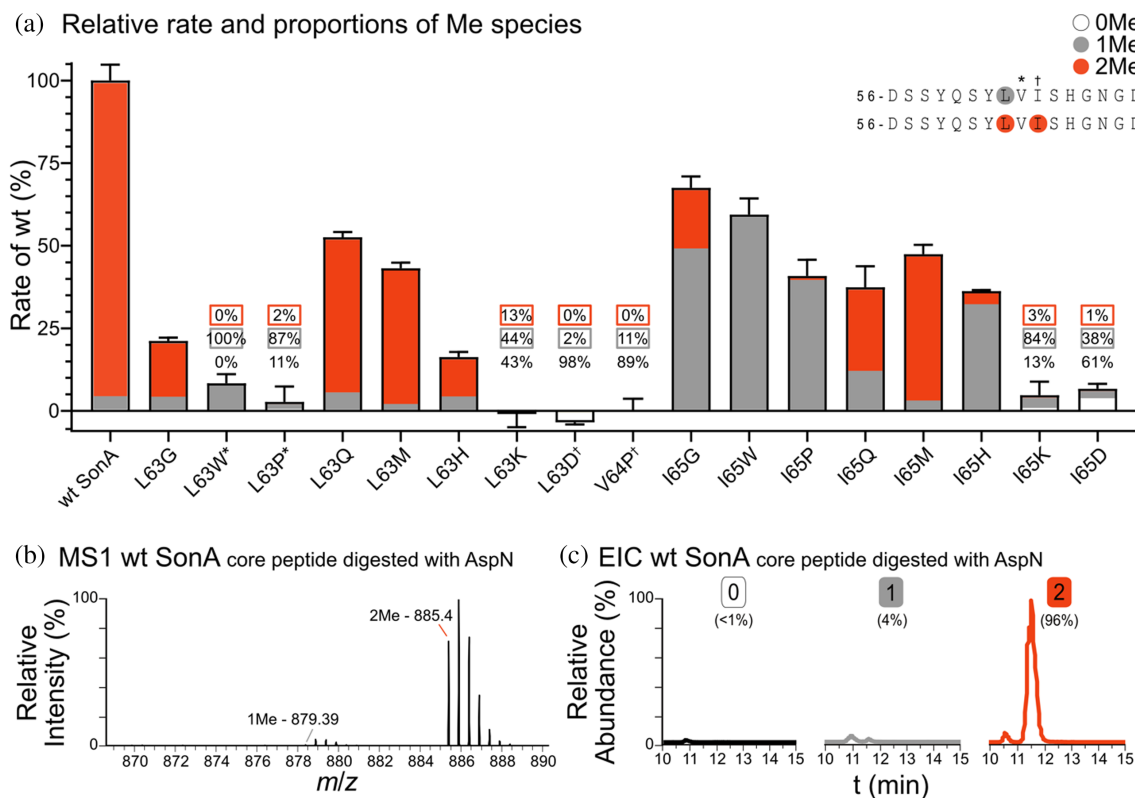
FIGURE 2 Relative rates and proportions of methylated species. (a) The rate of each SonA variant assayed with wt SonM is normalized to the rate of wt SonA and wt SonM (100%). The y-axis shows the mean-normalized rate plotted with the standard deviation amongst replicates, and the x-axis denotes the SonA variant assayed. Each bar in the graph shows the relative abundance of each methylated species observed by LC–MS/MS after 16 h from an in vitro reaction. White bars represent the fraction of peptides observed with zero methylation, gray bars represent mono-*N*-methylation, and orange bars represent bis-*N*-methylation. The methylation positions for each methylated species are circled within the sequence following the same color scheme. An asterisk (*) indicates a shift in mono-*N*-methylation position to V64. A dagger (†) indicates a shift in the mono-*N*-methylation position to I65. (b) Representative MS1 spectrum of wt SonA after a 16-h in vitro reaction with wt SonM and AspN digest. The y-axis shows relative intensity and the x-axis the mass-to-charge (*m/z*) value. The *m/z* values corresponding to the mono-*N*-methylated (gray) and bis-*N*-methylated (orange) peptides are labeled. (c) The extracted ion chromatogram (EIC) of wt SonA after a 16-h in vitro reaction with wt SonM. The relative abundance of each methylated species identified in the MS1 data is plotted vs. the retention time. The relative area under the curves were used to determine the methylation proportions plotted in (a) for all variants. The EIC for AspN-digested fragments with zero methylation are shown in black, mono-*N*-methylation in gray, and bis-*N*-methylation in orange.

LC–MS/MS to verify regiospecific methylation at each site (Figure 2b,c).

Generally, modifications at the first methylated position, X63, caused greater reaction rate attenuation when compared to the synonymous substitution at X65 (Figure 2a). However, when methylation was observed in these variants, it was preferentially observed on X63, the first site of methylation (Figure S1a,f,g,u,v,y,z,ac,ad,ag–ai). Tryptophan, presumably due to steric interactions, and proline, a tertiary amide, caused a positional shift in methylation, where the majority of methylated product was observed at V64 (Figures 2a and S1j,l–n). L63D was our only variant from this group to show 98% unmethylated peptide after overnight incubation. L63K also produced lower relative proportions of mono- and

bis-*N*-methylated species at 44% and 13%, respectively (Figures 2a and S1a,ag–ai,am,an). Our results suggest charged amino acids are poorly tolerated at the *i* and *i* − 2 positions, likely because of the hydrophobic binding pockets observed in our wt SonM•SonA crystal structures (Figure S2).

While variation at X65 generally resulted in less rate attenuation, product analysis by LC–MS/MS showed a marked decrease in the abundance of bis-*N*-methylated species in all cases except methionine substitution. All X65 variants resulted in *N*-methylation of L63; however, methylation at X65 was poor or absent if the residue was charged or bulky or was proline (Figures 2a and S1a,k,o–q,ae,af,aj–al,ao–aq). The greatest rate decreases were observed when X65 was a charged residue, suggesting the

extended binding pocket for the $i + 2$ position is also less tolerant to charged residues (Figure S2). This contrasts with the I65W/P variants, which retain high rates of reaction (>50% compared to wt SonA), indicating that these residues are tolerated at the $i + 2$ binding pocket.

We also created SonA-V64P and found that SonM was less tolerant at this position compared to proline at either X63 or X65, as indicated by 86% unmethylated species after an in vitro overnight reaction. The small proportion of monomethylated peptide detected was methylated at I65 (Figures 2a and S1a,r–t). This result mimics an observation with OphMA variants. Previously, when residues V403, V406, or I407 were changed to proline within the core, N-methylation was never observed directly preceding the substituted proline but did proceed C-terminally on the core peptide. For example, OphMA-V403P showed no methylation N-terminal to the substitution but methylation on V404 or G405. OphMA-V406P and OphMA-I407P showed methylation on V401 and V403 but no evidence of methylation on the residue immediately preceding the proline (Song et al. 2020). We postulate that the restricted backbone angles from proline at P64 prevented methylation from occurring at L63.

2.2 | Structural insights towards point-variant effects

We examined the effects of this set of point variants by subjecting them to structural studies in the presence and absence of cofactor. All structure and refinement statistics are presented in Table S2. The structure of the SonM•SonA-L63D complex could be solved in absence of cofactor, as well as bound to SAH and SAM at 2.35, 2.3, and 2.0 Å resolution, respectively PDB IDs 9CH2, 9CH3 and 9CH5; (Table S2 and Figure S3). Notably, the data collected for crystals obtained in presence of SAH exhibit pseudosymmetry and twinning issues (Table S2). In all structures, SonM and SonA-L63D form a dimer of heterodimers that closely aligns to the previously solved wt SonM•SonA-2Me structures (Figure S3) (Miller et al. 2021). For instance, the complexes bound to SAH and SAM—SonM•SonA-L63D•SAH and SonM•SonA-L63D•SAM—show closed active-site loops, which have previously been designated as the "top lock" comprised of the top and side "clamps" (Figure S4) (Miller et al. 2021). Conversely, the complex crystallized in the absence of cofactor—SonM•SonA-L63D• ± SAH—shows the top and side clamps in open conformations (Figure S4). Only one of the two SonM molecules in the asymmetric unit is bound to SAH (chain A), and the unbound SonM exhibits an open "bottom lock" configuration (chain C), where the stacking interaction between
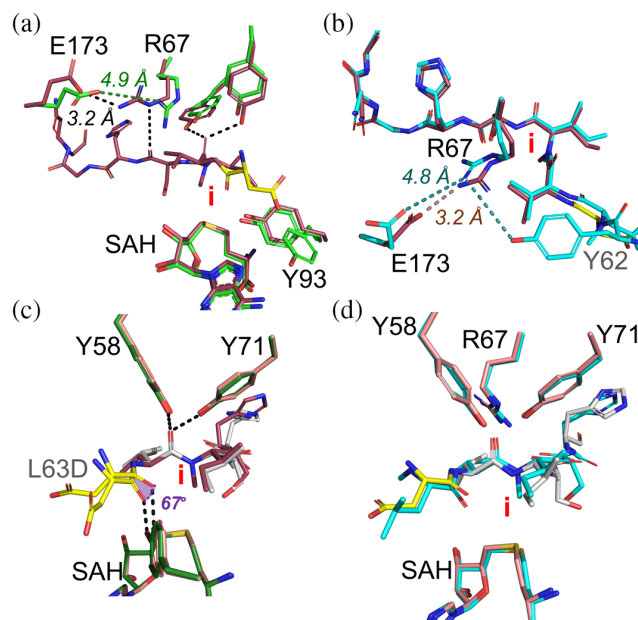
FIGURE 3 Structures of SonM and SonA-L63D highlight critical residues for core-peptide binding. (a) Superposition of SonM•SonA-L63D•SAH (PDB: 9CH3) and SonM•SonA-L63D• ± SAH (PDB: 9CH2) obtained in the presence and absence of SAH, respectively. Both are SAH-bound, but the core peptide is present in the SAH co-crystallized sample (chains A and B, maroon sticks) and absent in the other structure (chain A, green sticks). (b) Comparison between SonM•SonA-L63D•SAH (chains A and B, maroon sticks) and wt SonM•SonA-2Me•SAH (PDB: 7LTE) (chains A and B, cyan sticks). (c) Comparison between the monomethylated core peptide (chain B, maroon sticks) bound in one SonM•SonA-L63D•SAH active site (chain A, dark green sicks) and the unmethylated core peptide (chain I, white sticks) bound in another SonM•SonA-L63D•SAH active site (chain H, pink sticks). (d) Comparison between the unmethylated core peptide (chain K, white sticks) bound in the SonM•SonA-L63D•SAH structure (chain J, pink sticks) and the bound bismethylated core peptide (chains C and D, cyan sticks) from the wt SonM•SonA-2Me•SAH complex (PDB: 7LTE). In all panels, the aspartic acid substitution within the core peptide is colored yellow. SonA residues are labeled in gray.

W166 and F99 is lost (Figure S4). Notably, both the SonM•SonA-L63D• ± SAH and SonM•SonA-L63D•SAH structures feature a zinc cation bound at the dimer interface, while SonM•SonA-L63D•SAM does not (Figure S3). The core peptide could be partially modeled in all SonM molecules in SonM•SonA-L63D•SAH (chain B: 8 residues, chain D: 6 residues, chain I: 6 residues, chain K: 5 residues), partially modeled in one of the SonM•SonA-L63D•SAM monomers (chain D: 4 residues), and not modeled at all in the SonM•SonA-L63D• ± SAH structure (Figures S3 and S4). Only one of the observed SonM molecules in this suite of structures is bound to a monomethylated core (SonM•SonA-L63D•SAH chains A & B,

position i). Inspection of the electronic density shows a density peak at the expected position for a methyl group between the peptide (position i) and the cofactor, and therefore this peptide fragment was modeled as mono-methylated (Figure S5b). No corresponding density peaks could be observed for the other modeled cores. This could be because they are unmethylated, or because of the limitations of the structure: all other cores are less well defined in the maps (and consequently shorter fragments are modeled) and this could explain the absence of peaks. We note that the interpretation of these maps is complicated by partial occupancy, data issues due to twinning, and consequently reduced quality maps. A detailed analysis of active-site lock configurations, metal binding, and core peptide conformations for all captured states of structures introduced in this paper will be fully discussed in a subsequent publication.

The SonM•SonA-L63D suite of structures highlights the previously hypothesized importance of specific active-site residues, namely SonM-R67, SonM-E173, and SonM-Y93. Indeed, the comparison of SonM•SonA-L63D• ± SAH, with no bound core peptide, and SonM•-SonA-L63D•SAH, where the core is bound, presents us with a unique opportunity to delve into the conformational changes induced by the binding of the core peptide. The comparison of the two structures reveals the mobility of SonM-Y93, which is implicated in cofactor binding and exchange (Miller et al. 2021) (Figure 3a). It also highlights the conformational change of SonM-R67, an essential residue for activity (Miller et al. 2021), which largely rearranges upon core binding and establishes a salt bridge with SonM-E173 (Figure 3a). The configuration of SonM-R67 is similar but not identical to its configuration in the wt complex. A comparison of the structures highlights the impact of SonA-Y62 on the hydrogen-bonding network established by SonM-R67, including with SonM-E173 (Figure 3b). In addition to the unfavorable electrostatic interactions between the hydrophobic binding pocket of SonM and the side chain of L63D, the comparison between the unmethylated and monomethylated cores in the SonM•SonA-L63D•SAH active sites indicates that another effect of this mutation could be to alter the angle of the $i-2$ carbonyl group in a mode that sterically hinders the presence of a methyl group at position i (Figure 3c). Interestingly, the unmethylated core peptide adopts a conformation that is similar to the conformation observed for the bis-N-methylated peptide in the wt SAH-bound complex (Figure 3d). Combined with the previous observation of the unmethylated core in a fully helical conformation (Miller et al. 2021), it suggests that the core peptide can, in the context of SonM's active site, oscillate between multiple structural states.

The SonM•SonA-L63D•SAM complex allowed for partial modeling of the core peptide (chain D: 4 residues). We note that this is the first time across the efforts presented here and previously published by our team (Crone et al. 2023; Miller et al. 2021) that a fragment of the core could be modeled when SAM is bound. This challenge in observing a discrete conformation of the core in the electronic density in presence of SAM may suggest that the core peptide probes the active site, or that in our crystallization conditions, has been fully methylated and is located outside of the binding cleft. In the SonM•SonA-L63D•SAM structure, while the electronic density maps suggest partial occupancy (Figure S6), it clearly reveals that the core peptide backbone is not aligned with the cofactor. Indeed, in all previous structures, including the SonM•SonA-L63D•SAH active sites where the unmethylated core is bound, SonA-I65 is bound at the i position with the Nα of I65 across from SAH (Figure 4a). In the SonM•SonA-L63D•SAM structure, there is no obvious Nα facing the cofactor (Figure 4b). This configuration could therefore correspond to a captured binding intermediate of the core rearranging and probing the active site for productive binding.

The structure of SonM in complex with SonA-I65W was also solved in the absence of cofactor, as well as bound to SAH and SAM at 2.65, 2.2, and 2.1 Å resolution, respectively PDB IDs: 9CGW, 9CH0 and 9CH1; (Table S2 and Figure S7). Here too, the data collected for crystals obtained in presence of SAH exhibit pseudosymmetry and twinning issues (Table S2). In the absence of cofactor, SonM•SonA-I65W crystallized in an apo state, with no bound cofactors or core peptides visible in either active site. The structure exhibits a zinc cation bound at the dimer interface (Figure S7). The top locks are in an open configuration, while one bottom lock is open (chain A) and the second appears distorted (chain C) (Figure S8). When crystallized in the presence of SAM (SonM•SonA-I65W•SAM), both SonM molecules (chains A and C) are occupied with the cofactor, with closed bottom locks and a bound zinc cation (Figures S7 and S8). The top locks are closed, yet the core peptide is also absent from the electronic density maps. In the presence of SAH (SonM•SonA-I65W•SAH), the SonM bottom locks are similarly closed (chains A, C, H, and J), and a bound zinc cation is also present (Figures S7 and S8). The core peptides could be partially modeled for three out of the four SonA molecules (chain B: 7 residues, chain I: 4 residues, chain K: 4 residues), with only one core (chain B) where monomethylation (position i) could be observed (Figure 4d). Overall, the difficulty to observe the core peptide in the electronic density maps suggests a high degree of conformational flexibility.
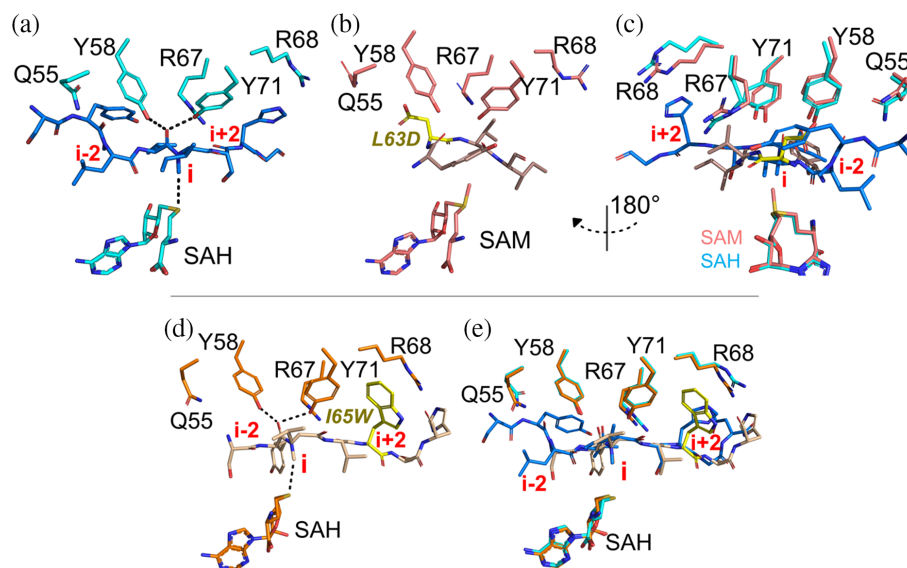
FIGURE 4 Comparison of binding position of SonA variants with wt in the SonM active site. (a) Binding of the wt SonA-2Me core (chain D, dark blue sticks) in wt SonM (chain C, cyan sticks) (PDB: 7LTE). (b) Unproductive binding of SonA-L63D core (chain D, beige sticks) into wt SonM (chain C, salmon sticks) (PDB: 9CH5). (c) Comparison between the wt SonM•SonA-2Me•SAH complex (chains C and D, cyan and dark blue sticks; 7LTE) and the SonM•SonA-L63D•SAM complex (chains C and D, salmon and beige sticks; 9CH5). (d) Binding of SonA-I65W•SAH core (chain B, beige sticks) in wt SonM (chain A, orange sticks) (PDB 9CH0). (e) Comparison between the wt SonM•SonA-2Me•SAH complex (PDB: 7LTE) (chains A and B, blue and cyan sticks) and SonM•SonA-I65W•SAH complex structures (chains A and B, orange and beige sticks; 9CH0). In panels b–f, the mutated core residue is colored yellow.

The electronic density for the core-peptide side chains in the SonM•SonA-I65W•SAH structure lacks the details to observe several side chains, including that of I65W. It is important to consider that these maps are affected by data twinning and are less detail-rich than expected. However, the maps allow us to place the peptide chain, and the region around residue I (L63) is particularly well defined (Figure S9a). The electron density also shows a density peak at the expected location for a methyl group on the backbone of residue L63 (Figure S9b). Since this observation corroborates the mass spectrometry data showing that SonA is mono-*N*-methylated on L63, the core peptide was modeled as mono-*N*-methylated. The overall conformation of the visible core fragment appears similar to the bismethylated core bound in the wt SonM•SonA-2Me•SAH complex. This configuration is expected for a few reasons: (i) the recognition for the side chain is fairly unspecific (i.e., hydrophobic residues), and (ii) the modeled fragment is centered on the catalytic site, and productive binding is constrained by the enzyme's chemistry. Structures show possible active site residue configurational changes (Figure 4e), including for SonM-Q55, SonM-R67, and SonM-R68, when comparing this novel structure to the previously determined SonM–SonA-2Me–SAH structure. However, the weak electron density for the side chain of R67 in particular does not provide strong support to interpret these variations.

One complex in the asymmetric unit of the SonM•-SonA-I65W•SAH structure does not show a bound core peptide (chains C and D). This provides an opportunity to compare this unbound structure to the wt SonM•-SonA-2Me•SAH complex. This comparison allows us to further examine the importance of the binding of the core on SonM active site reconfiguration (Figure S10). Comparison of the two structures highlights conformational changes of the previously identified SonM-Q55, SonM-R67, and SonM-R68 residues and identifies that SonM-L34, SonM-E173, and SonM-F179 may also play important roles in core-peptide binding. However, the potential role(s) of R67, R68, and F179 should be cautioned by the weak density supporting their modeled conformations. We do note that this comparison highlights the potential interactions between SonM-R67 and SonM-E173, which were previously designated as part of the "top lock," an interaction network likely governing active site clamp movement (Miller et al. 2021).

2.3 | SonA-Y62 determines methylation at SonA-L63

Maintenance of SonM regiospecificity for the first *N*-methylation at SonA-L63 is notable. In addition, we have previously shown that deletions to the fifth helix of the
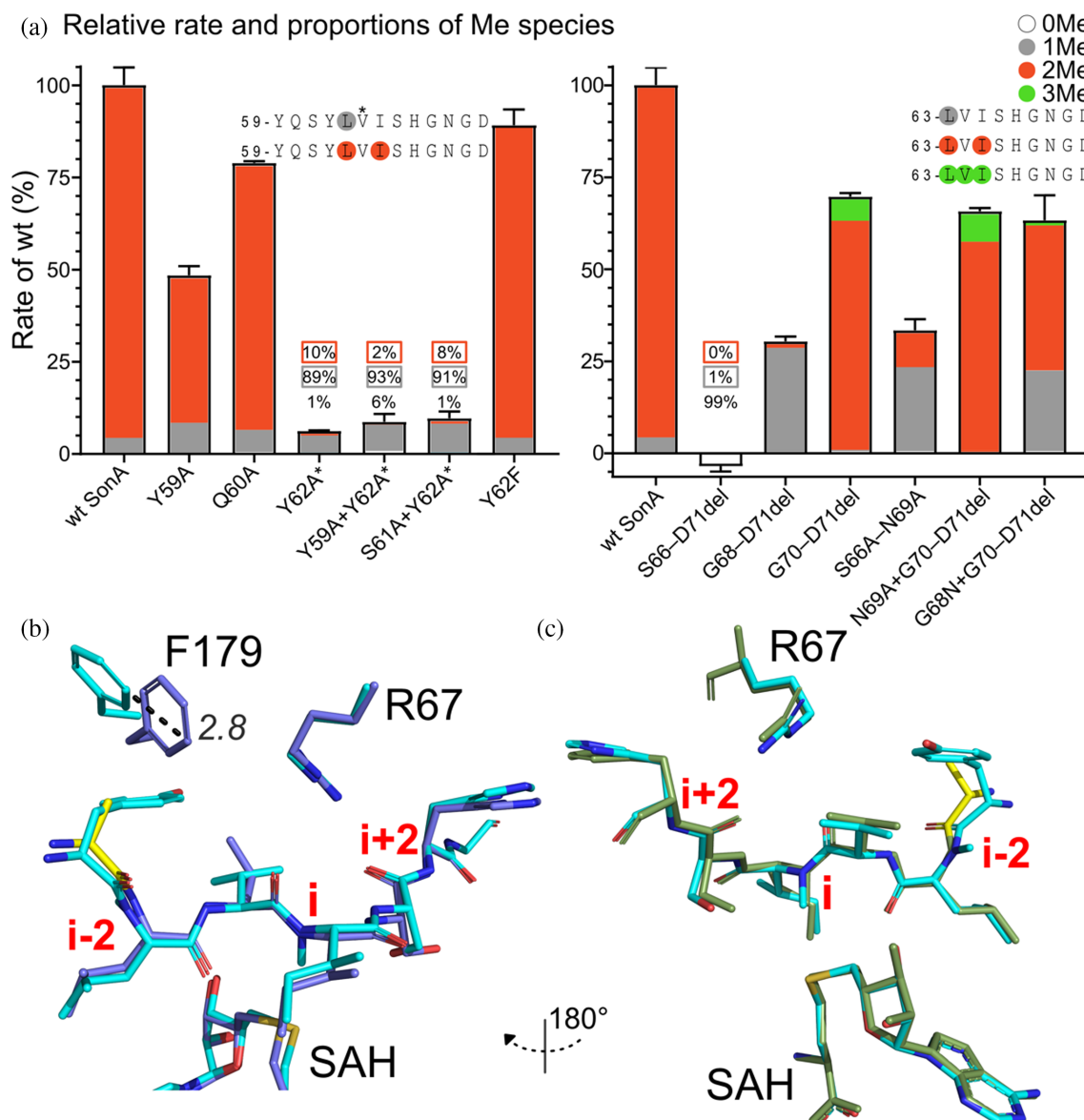
FIGURE 5 Relative rate and proportions of methylated species from SonA variants. (a) The rate of each SonA variant assayed with wt SonM is normalized to the rate of wt SonA and wt SonM (100%). The y-axis depicts the mean-normalized rate plotted with the standard deviation amongst replicates, and the x-axis denotes the variant assayed. Each bar represents the relative abundance of each methylated species observed after 16-h in vitro reactions by LC–MS/MS. White bars represent the fraction of peptides observed with zero methylation, gray bars represent mono-*N*-methylation, orange bars represent bis-*N*-methylation, and green bars represent tris-*N*-methylation. The methylation positions for each methylated species are circled within the sequence following the same color scheme. An asterisk (*) indicates a shift in mono-*N*-methylation position to V64. Structure of the SonM SonA-Y62A complex sheds light on core peptide binding and recognition. (b) Comparison between the unmethylated core (i) (chain D, dark blue sticks) from the SonM•SonA-Y62A• ± SAH structure (PDB: 9CH7) with the bismethylated wt core from the SonM•SonA-2Me•SAH (chain D, cyan sticks sticks; PDB: 7LTE). (c) Comparison between the monomethylated core (chain H, green sticks) from SonM•SonA-Y62A•SAH (PDB: 9CHI) and the bismethylated wt core from the SonM•SonA-2Me•SAH (chain D, cyan sticks; PDB: 7LTE). In panels (b) and (c), the substituted alanine is colored yellow.

BBD do not alter regiospecificity and result in only subtle rate decreases. However, deletions immediately N-terminal to the first methylation site, SonA-Q60–Y62, result in an undetectable reaction rate and a shift in the methylation pattern to I65 (Crone et al. 2023). Here, we chose to investigate this region further by alanine-

scanning positions N-terminal to L63. SonA-Y59A and SonA-Q60A variants resulted in mild rate decreases and retention of the native methylation pattern (Figures 5a and S11a–h). However, SonA-Y62A caused a dramatic rate decrease and shift in the methylation pattern. After 16 h, about 89% of the sample was mono-*N*-

methylated (Figures 5a and S11a,i–k). The major species showed *N*-methylation of V64 and a minor species at I65. This change in methylation position implicates Y62 in recognition of the SonA core peptide for the first methylation event. To determine possible additive effects with other SonA amino acid substitutions, we created the double-residue variants SonA-Y59A + Y62A and SonA-S61A + Y62A. Both variants performed comparably to the SonA-Y62A variant in all aspects, including reaction rate, methylation position, and relative abundance of methylated species (Figures 5a and S11a,l–r). To further assess if the hydroxyl of Y62 could be important for recognition, we created and assayed SonA-Y62F. However, SonA-Y62F displayed rates almost identical to wt (89%) and methylation predominantly on L63 and I65 after 16 h (Figures 5a and S11a,s–x). This indicates that the hydroxyl of SonA-Y62 is of minimal importance, but the size of the SonM-X62 side chain is pivotal for SonA recognition and methylation. From the structure of the SonM•SonA-I65W•SAH complex, we hypothesize that SonA-Y62 induces rotamer movement of SonM-F179, which is important to core-peptide positioning in the active site. Mutation of SonM-F179 to alanine resulted in impairment to core processing, with only 78% bis-*N*-methylated species observed after a 16-h reaction (Figure S12).

Structural investigation into the role of SonA-Y62 in determining methylation on the subsequent residue justified crystallization of wt SonM with the SonA-Y62A variant. Here again, the structure of the SonM•SonA-Y62A complex was solved in absence of cofactor, as well as bound to SAH and SAM at 2.2, 2.2, and 1.5 Å resolution, respectively PDB IDs 9CH7, 9CHI and 9CHK; (Table S2 and Figure S13). The data collected for crystals obtained in presence of SAH exhibit pseudosymmetry and twinning issues (Table S2). In the absence of cofactor during crystallization, the complex (SonM•SonA-Y62A• ± SAH) was solved with four copies of SonM—two of which are bound to SAH (chains C and E), present closed bottom locks, and have closed top locks with a partially resolved core (Figure S14). In one of these two copies, only two core residues are visible (chain F), whereas nine amino acids could be modeled for the second copy (chain D) (Figure S15). The other two SonM molecules present in the asymmetric unit are unbound to cofactor (chain A and G), present open bottom locks, and have open top locks without a core peptide bound in the active site (Figures S14). A zinc cation is not visible in these structures (Figure S13). The structure obtained in the presence of SAH (SonM•SonA-Y62A•SAH) is fully occupied with SAH, with closed bottom locks, a resolved core in all SonM molecules, closed top locks, and no bound zinc cation. In the presence of SAM, the structure (SonM•SonA-Y62A•SAM) shows a fully occupied SAM-bound

complex, with closed bottom locks, no visible core, closed active-site loops, and also no bound zinc cation (Figures S14).

In the SonM•SonA-Y62A•SAH complex, the SonA core could largely be resolved (chains B, D, and H: 9 residues, chain F: 8 residues) and is modeled as mono-*N*-methylated on the I65 residue (chains B, F, and H) (Figure S16a). This structure is also affected by data twinning/pseudosymmetry, and map quality is affected. Yet, a density peak for the *N*-methyl group is clearly visible in a polder omit map (Figure S16b). This contrasts with our LC–MS/MS data, where the predominant methylated species is on V64, and therefore indicates crystallization selected a minor species. The determination of the SonM•SonA-Y62A• ± SAH complex captured an unmethylated core peptide in the SonM active site (chain D) (Figure 5b). When compared to the wt SonM•SonA-2Me•SAH complex, it adopts a relatively similar conformation, with the Nα of I65 across from SAH. Further comparison reveals SonA-Y62 largely affects the conformation of SonM-F179, and to a lesser extent, SonA-V64 (Figure 5b). As previously observed in the SonM•SonA-I65W•SAH complex, SonA-Y62 also affects the position of SonM-R67 (Figure S10). The change in position is also apparent when compared to the monomethylated core (chain H) observed in the SonM•SonA-Y62A•SAH complex and the bismethylated core bound in the wt complex (Figure 5c). These structural variations clearly highlight the key role of Y62 in SonM recognition of the core, and these observations largely corroborate the observed effects of the Y62A variant on the methylation patterns.

2.4 | The C-terminus of SonA influences iterative activity

Previous studies with the fused borosin precursor OphMA have shown that truncations to the C-terminus result in incomplete methylation of the core peptide (Song et al. 2018; Song et al. 2020). We sought to understand the influence of the six amino acids proceeding *N*-methylation at the C-terminus of SonA. Three SonA C-terminal truncations were initially created to test their influence on SonM activity and regioselectivity. When all six amino acids following SonA-I65 are removed (construct SonA-S66–D71del), the reaction rate was undetectable via our continuous assay. The MS1 EIC showed 98% unmethylated peptide after overnight reaction. With truncation of four C-terminal amino acids (construct SonA-G68–D71del), we observed recovery of ∼30% of the wt rate with 96% of the mono-*N*-methylated species observed on residue SonA-L63. Finally, the two-residue deletion variant SonA-G70–D71del recovered ∼70% of the wt rate, with ∼89% bis-*N*-methylated species and our
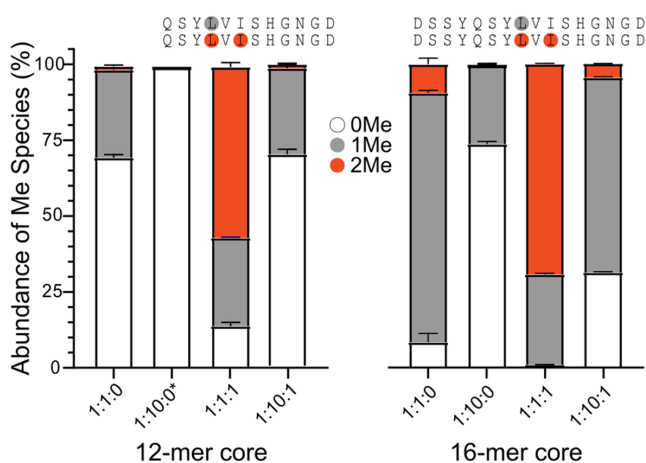
FIGURE 6 Relative proportions of methylated species. The y-axis shows the mean relative abundance and standard deviation of each methylated species for either the 12-mer or 16-mer peptide assayed. The x-axis denotes the ratios of each component used in the reaction (SonM:peptide:BBD). Reactions were performed in duplicate (* was not performed in technical duplicate), quenched after 24 h, and analyzed by LC–MS/MS. White bars represent the fraction of peptides observed with no methylation, gray bars represent mono-*N*-methylation, and orange bars represent bis-*N*-methylation.

first observance of ~9% tris-*N*-methylated species on SonA-L63, -V64, and -I65 (Figures 5a and S11a,y-aj).

Next, we constructed and tested several single residue substitution variants in combination with various deletion variants (Figures 5a and S11a,ak-ax). Deletion of SonA C-terminal residues G70 and D71 (S66–D71del, G68–D71del, N69A + G70–D71del, G68N + G70–D71del) results in decreased overall methylation rates as well as reduced SonM fidelity, with several variants displaying methylation on SonA-V64. Variation or deletion of G68 and N69 (S66–D71del, G68–D71del, S66A–N69A, N69A + G70–D71del, G68N + G70–D71del) also generally resulted in reduced rates, especially for the second methylation on SonA-I65. While no single residue is entirely responsible for regiospecificity, the position of the asparagine and presence of G70–D71 help select for I65 methylation. These results suggest that the C-terminal residues "GNGD" influence the pattern and degree of SonA methylation. Notably, this sequence is conserved across many SonA homologs within the genus *Shewanella* (Miller et al. 2021). Concomitantly, we designed and tested SonM-R68A. Assay of this variant with wt SonA resulted in 80% mono-*N*-methylated peptide and 4% bis-*N*-methylated peptide (Figure S12). Previously, we noted that R68 is part of the network of hydrogen bonding interactions that close the top and side clamps of the top lock, and we have observed hydrogen

bonding with SonM-R68 and the C-terminus of SonA (Miller et al. 2021). While removal of the guanidinium group affects the efficiency of both methylation events, the data show a more drastic effect for the second methylation. This supports our observation that R68 forms a hydrogen bond with the C-terminus of SonA and may assist in positioning for the second methylation event.

2.5 | A minimal core peptide substrate for methylation

Through defining core peptide boundaries required for maximal SonM activity, we hypothesized SonM could methylate peptides in trans to, or in the absence of, the BBD. We tested the 12-mer core "QSYLVISHGNGD" and the 16-mer "DSSYQSYLVISHGNGD" with SonM in the presence or absence of the BBD (SonA 1–55) in 24-h in vitro assays (Figures 6, S17, and S18). While far slower than reactions with wt SonA, the 16-mer core peptide was universally more tolerated than the shorter 12-mer peptide. Upon 10:1 molar excess of peptide to SonM, methylation was substantially inhibited, with 99% and 73% unmethylated 12-mer and 16-mer core peptides observed, respectively (Figures 6, S17a,k, and S18a,k–m). However, in-trans addition of the BBD at a 1:1 mole ratio with SonM resulted in considerably higher fractions of mono- and bis-*N*-methylated species with the peptide substrates. After 24 h, we maximally observed 30% mono-*N*-methylated and 69% bis-*N*-methylated species with the 16-mer peptide in equal mole ratios with SonM and the BBD (Figures 6 and S18a,e–g). These experiments suggest that, when tethered, the BBD not only provides an increased local concentration effect for catalysis, but may also activate the enzyme towards the substrate. Future work will attempt to disentangle the mechanism of activation. These data provide additional evidence that regiospecificity is predominantly determined by SonM interactions with the core peptide.

2.6 | Core peptide secondary-structure requirements

The work presented thus far aimed to define important residues for core recognition and positioning. However, the previously published crystal structure of the SonM-R67A–SonA-0Me complex (PDB code: 7LTS) captured the unmethylated SonA core peptide as an α-helix in the active site before top lock closure. Consequently, we proposed that secondary structure may be guiding the direction of iterative activity. *N*-Methylation could force segmented helix-breaking and drive core peptide

repositioning for subsequent methylation events. However, all unmethylated and monomethylated core peptides resolved in the complexes presented in this manuscript are unstructured. This could either represent a later stage in binding for catalysis, with top lock closure and helix dissipation, or negate the necessity for helix formation. While it is difficult to disentangle sequence specificity from secondary-structural changes (Chou and Fasman 1974; Levitt 1978), we aimed to address enzymatic requirements for iterative activity with an alternative series of core peptide replacements. First, we appended a well-characterized sequence of known helicity "AAQAAAAQAAAAQAAY" (Scholtz et al. 1991) with no significant sequence similarity at the C-terminus of the SonA BBD to create the construct SonA-G55insAH. In addition, we assayed two similar sequences with varying retention of the SonA linker, SonA-G55insQSYAH (QSYQAAAAQAAAAQAAY) and SonA-Y62insAH (DSSYQSYQAAAAQAAAAQAAY). When incubated with wt SonM, all three constructs resulted in undetectable activity by the continuous assay (Figure S19). Only the SonA-Y62insAH variant showed discernible methylation with 11% mono-N-methylated species on Q63 after the 16-h reaction (Figures S19 and S20a,g). This result emphasizes the importance of the sequence upstream of methylation in positioning for the first methylation event.

In order to find and test similar SonA core sequences with known secondary structure, we wrote two custom scripts (Code S1 in Data S1). The first enables a user to search the PDB for entries containing a designated sequence motif and returns associated IDs. The second script uses Rosetta (Chaudhury et al. 2010) to determine what the secondary structure is for the queried sequence within each structure file. We surveyed the PDB for different secondary structures using the degenerate sequence motif "[D/E]XXX[Q/A][S/T/A][Y/F]XXX." This motif retained the residues found most critical through our extensive mutational analysis or which were more broadly found in *Shewanella* borosin precursor homologs. The initial primary sequence search of the PDB found 12,185 unique entries. Of these, 6172 structures were successfully retrieved, analyzed, and found to contain a resolved structural segment matching the queried sequence motif. From this output, we selected four sequences that, when appended at the C-terminus of the SonA BBD, were also predicted by PSIPRED (Jones 1999) and AlphaFold2 (Jumper et al. 2021) to form helices (2) or coils (2) (Figure S21). After 16-h in vitro reactions, both the predicted helical core constructs and one coil construct showed a majority of mono-N-methylation at the X63 position (Figures S19 and S20a,h,l,m,q–t,x–z).

These non-native core sequences were assayed in tandem with triple residue substitution variants, containing only L63–I65 sequences swapped out for the corresponding non-native residues (Figures S19 and S20a,i–k,n–p,u–w, aa–ac). Unfortunately, for these data we are unable to predict active-site-associated secondary structural changes of the selected core peptides and how this may be influencing positioning for catalysis. While these data again emphasize the importance of the sequence upstream for the first methylation, it does not clearly support the requirement for specific secondary structures for iterative catalysis.

2.7 | Engineering SonA variants for increased methylation

With our newly acquired understanding of regiospecificity for methylation, we designed five SonA variants to yield different bis-, tris-, and tetrakis-N-methylated peptides. We varied aspects of the core peptide in several ways: (1) by extending the hydrophobic region where methylation occurs (SonA-I65insVLVI); (2–4) by duplicating varying regions of the core with different intervals (SonA-Y62–S66dup + G70–D71del, SonA-Y62–G68dup + G70-D71del, SonA-S61–N69dup + G70–D71del, respectively); and (5) by entirely duplicating the core peptide to mimic type V borosins (SonA-D56–G70dup) (Imani et al. 2022). With each set of insertions lengthening the core, we saw increasing activity. Variants 4 and 5 performed at ~38% and 75% of wt, respectively (Figure 7). After overnight in vitro reaction, we see a similar trend, where variants 4 and 5—retaining more of the native sequence in the duplicated regions—have higher proportions of tris- and tetrakis-N-methylated species in the predicted positions from our wt substrate (Figure S22a,l–z).

Variants 1 and 2, with fewer duplicated residues between predicted methylation sites, are poorer substrates for the enzyme as noted by slower relative rates (Figure 7). We also observed unpredicted methylation patterns, where valine is methylated prior to the first leucine (Figure S22b–g). From assays of SonA-Y62F and alignments of other SonA homologs, we see that F/L/I can alternatively occupy the $i - 1$ position. This provides a possible explanation that consecutive hydrophobic residues could compete for misalignment. Surprisingly, the isoleucine residues are not methylated in these variants (Figures 7 and S22b–g). Variant 3 contained the shortest duplication (seven residues), where we observed the return of the native methylation pattern on the first repeat. However, we still see a majority of unmethylated
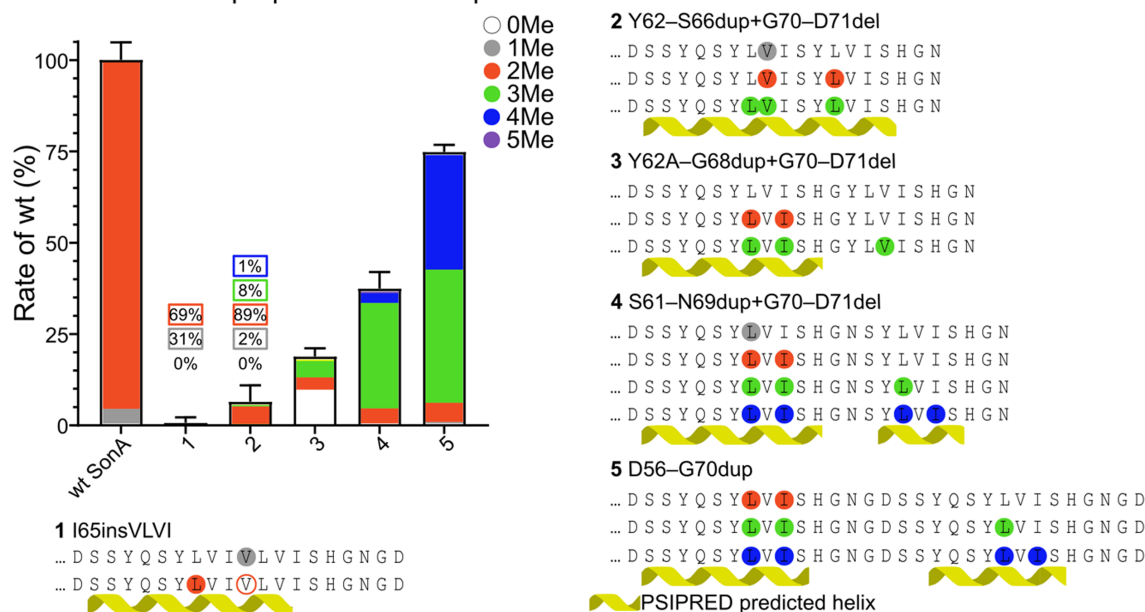
FIGURE 7 Relative rate and proportions of methylated species (a). The rate of each SonA variant assayed with wt SonM is normalized to the rate of wt SonA and wt SonM (100%). The y-axis shows the mean-normalized rate plotted with the standard deviation amongst replicates, and the x-axis denotes the variant assayed. Each bar shows the relative abundance of each methylated species observed after 16-h in vitro reaction by LC–MS/MS. White bars represent the fraction of peptides observed with no methylation, gray bars represent mono-*N*-methylation, orange bars represent bis-*N*-methylation, green bars represent tris-*N*-methylation, blue bars represent tetrakis-*N*-methylation, and purple bars represent pentakis-*N*-methylation.

peptide after 16 h, indicating that the unmethylated substrate is challenging for the enzyme to position for catalysis (Figures 7 and S22h–k). Notably, when we predict the secondary structure of these non-native core peptides with PSIPRED (Jones 1999), we see a trend where the two most efficiently processed variants 4 and 5 have two predicted helices at the sites of methylation, while the other three variants have one predicted helix.

3 | CONCLUSION

The ability to predict and tailor modifications in RiPP biosynthetic pathways is still in its infancy. Several binding modes have been observed in RiPP precursor interactions, with some specific to domains within the leader, some with diffuse binding across both leader and core, and some where specific modified-core interactions facilitate recognition (Montalbán-López et al. 2021). Amongst others, lanthipeptide, cyanobactin, graspetide, and lasso peptide biosyntheses have extensively been characterized (Chatterjee et al. 2006; Cheung et al. 2010; Goto et al. 2014; Khusainov et al. 2013; Kuipers et al. 1996; Mavaro et al. 2011; Rink et al. 2007; Sardar et al. 2015a; Sardar, Pierce, et al., 2015; Weiz et al. 2011; Ziemert

et al. 2008). Understanding of binding and recognition mechanisms along with substrate scope has enabled the production of peptide libraries for bioactivity screening and has facilitated the first attempts at producing chimeric precursor peptides for recognition by modifying enzymes from different RiPP families (Burkhart et al. 2017; Franz and Koehnke 2021; Reyna-González et al. 2016; Sarkar et al. 2022; Thokkadam et al. 2023; Yang et al. 2018). Notably, the majority of the best-characterized examples reveal that modifying enzymes react with the side chains of specific residues. Thorough research into other RiPP families, including those that involve iterative backbone modification like epimerization and *N*-methylation, is needed to facilitate creation of more diverse, bioactive peptide libraries (Vagstad 2023).

In this work, we presented a detailed structural analysis and extensively probed the substrate scope of the *N*-methyltransferase SonM. Active-site complementarity to the core sequence is maintained without specific side-chain interactions beyond size and hydrophobic interactions. While SonM has sequence requirements for regiospecific methylation, we show that the substrate retains plasticity to permit production of diverse methylated peptides, even untethered to the BBD leader peptide. This work is proof of concept for the utility of the first characterized discrete

amide-backbone *N*-methyltransferase towards non-native applications. The major contribution to core binding comes from the top clamp (SonM 172–182) and side clamp (SonM 58–68), which appear to be highly dynamic from the diverse positions they occupy in all of our crystal structures. In concert, it is likely that precursor dynamics play a role in binding, positioning, and release. Despite the lack of additional evidence for required secondary structural elements, our suite of crystallographic data shows that the unmethylated core is dynamic within the context of the active site. We posit that the core peptide must undergo extensive conformational sampling to position it correctly for top and side clamp closure, as would be necessary for proper packing prior to catalysis, with redundant recognition elements facilitating core-peptide positioning within the active site. Future structural analyses with SonA and SonM or other borosin systems will further elucidate these interactions to grant a more complete iterative catalytic cycle of borosin peptide *N*-methylation.

4 | METHODS

4.1 | Materials

Unless otherwise stated, all chemicals were purchased from Sigma-Aldrich, enzymes from New England Biosciences, and primers from Integrated DNA Technologies. Analysis software(s) used are mentioned in each section. Affinity Designer v1.10 was used to make the figures in this manuscript.

4.2 | Cloning

Previously designed plasmid expression constructs of *his₆-sonM*, *his₆-sonA*, or *sonM + his₆-sonA* (Miller et al. 2021) were used as templates. Appropriate primer pairs (Table S1) introduced the mutation by PCR as described previously (Crone et al. 2023) using Q5 DNA polymerase. Reactions were performed following manufacturer's protocols: initial denaturation of 30 s at 98°C; denature 10 s at 98°C, anneal (temperature varied) for 20 s, 4-min extensions at 72°C for 30 cycles; final extension for 2 min at 72°C. The samples were then treated with DpnI to remove the plasmid template and purified using the GeneJET PCR purification kit (Thermo Scientific). The linear DNA fragment was then phosphorylated by T4 polynucleotide kinase (Thermo Scientific) and the sample purified using the same kit. The phosphorylated, linear DNA was then ligated with T4 DNA ligase and transformed into TOP10 cells. The open reading frame was sequence-verified by ACGT.

4.3 | Protein expression and purification

Sequence-verified plasmids were transformed into BL21 (DE3) cells, and a single colony was used to inoculate 10-mL cultures of LB (Research Products International). The cells were cultured overnight at 37°C shaking at 220 rpm. The following day, cultures were used to inoculate 1 L of Terrific Broth (Research Products International) in 2.5-L baffled expression flasks (Thomson Scientific). The expression cultures were incubated at 37°C shaking at 220 rpm until the optical density at 600 nm (OD_{600}) reached ∼2.0. The expression cultures were then placed in ice for 30 min followed by induction with 200 μM IPTG (final concentration). The cultures were then incubated for 24 h at 16°C shaking at 220 rpm. Cells were harvested by centrifugation for 30 min at 5000*g*, flash frozen in liquid nitrogen, and stored at −80°C until purification.

Frozen cell pellets were resuspended in lysis buffer (50 mM HEPES pH 8, 300 mM NaCl, 10% glycerol) with 20 mM imidazole at a ratio of 4 mL of buffer per gram of cell mass. After manual resuspension of the cell pellet, lysozyme was added at a final concentration of 1 mg/mL and incubated on ice for 30 min. The cells were further lysed by sonication (Qsonica), and soluble and insoluble protein fractions were separated by centrifugation at 15,000*g* for 30 min. The supernatant was placed into a fresh tube and incubated with Nickel NTA agarose beads (Gold Biotechnology) for 1 h at 4°C on a rotator. Using a fritted, gravity-flow column, the resin was applied to the column, washed with lysis buffer, and the protein of interest was eluted with lysis buffer containing 250 mM imidazole. Protein purity was assessed by SDS-PAGE. Fractions containing the eluted protein of interest were pooled, concentrated with an Amicon Ultra Centrifugal Filter, and dialyzed into lysis buffer to remove imidazole. Proteins were flash frozen in liquid nitrogen and stored at −80°C.

The wt SonM enzyme, SonM enzyme variants, and the co-expression constructs for crystallography were additionally purified by size-exclusion chromatography using an AKTA FPLC system. Briefly, the protein was applied to HiLoad 16/600 Superdex 200 pg (Cytiva) pre-equilibrated with lysis buffer. A flow rate of 1 mL/min was used. Only fractions of highest purity were pooled, concentrated, and flash frozen for later use.

4.4 | Relative k_{cat} determination by coupled-enzyme assay

A coupled-enzyme assay was used to measure the rate of the methyltransferase reaction as previously adapted by

our lab (Crone et al. 2023; Miller et al. 2021). Briefly, 100-µL reactions were set up in a 96-well, flat-bottom plate (Sarstedt), where the reaction progress at 30°C was monitored by the absorbance at 340 nm in a SpectraMax iD5 plate reader (Molecular Devices). All coupled-enzyme assay components, 80 µM wt his_6-SonA or variant, and 1000 µM SAM (~97.5–98% purity; Miller et al. 2021) were added to the wells and allowed to equilibrate for 5 min. The reaction was started with the addition of 5 µM wt his_6-SonM. Reads were taken every 30–40 s. The rates were measured as the slope over the linear range. For activity to be measurable, it had to be above the background decomposition rate of SAM. SonA variant rates were normalized to the reaction of wt his_6-SonA with wt his_6-SonM at 100% and plotted in GraphPad Prism v10.1. All assays were performed in triplicate.

4.5 | In vitro reactions for analysis of substrate methylation patterns

Reactions were performed overnight in 50-µL reaction volumes at room temperature (~25°C). In a Protein LoBind tube, 80 µM his_6-SonA (or mutant), 8 µM SAHN, and 1 mM SAM were mixed in 50 mM HEPES buffer pH 8. The reaction was started with the addition of wt his_6-SonM at a final concentration of 5 µM. Reactions were quenched with 5x SDS-dye and boiled for 5 min. The reactions were then run on a 15% SDS gel for analysis by mass spectrometry.

Reactions with the core peptide were set up in 25-µL reaction volumes for 24 h at room temperature. Two synthetic peptides were purchased from GenScript at ≥98% purity. The 12-mer peptide "QSYLVISHGNGD" was dissolved in DMSO and then diluted into 50 mM HEPES buffer pH 8. The 16-mer peptide "DSSYQSYLVISHGNGD" was dissolved in 3% ammonium hydroxide and diluted into 50 mM HEPES buffer pH 8. In a Protein LoBind tube, 50 µM peptide, 8 µM SAHN, and 1 mM SAM were combined in 50 mM HEPES buffer pH 8. For indicated conditions, 50 or 5 µM of his_6-BBD-SonA was also included in the reaction. The reactions were started with the addition of either 50 or 5 µM wt his_6-SonM and quenched with 6 M urea (final concentration). The reactions were then vacuum-concentrated, resuspended in 0.1% formic acid, and C18 zip-tipped following the manufacturer's protocol.

4.6 | LC–MS/MS analysis of SonA variants

Samples were prepared for mass spectrometry by in-gel protein digest as previously described (Crone et al. 2023; Miller et al. 2021). Briefly, the protein band of interest was cut out of the gel, diced into ~1×1 mm cubes, and placed into a Protein LoBind tube. The gel pieces were washed in 15 min intervals with 50 mM ammonium bicarbonate and 50% acetonitrile until no coomassie stain remained. The gel pieces were then dehydrated with 100% acetonitrile and the acetonitrile was discarded. The appropriate protease, AspN or Trypsin (Promega), was prepared in 50 mM ammonium bicarbonate and added to the gel pieces. The gel pieces were allowed to rehydrate on ice for 15 min, additional buffer added to sufficiently submerge them, and then placed at 37°C overnight. The next day, all liquid was recovered to a new Protein LoBind tube. The digested peptides were then extracted from the gel pieces with increasing concentrations of acetonitrile: 50% acetonitrile with 0.3% formic acid, 80% acetonitrile with 0.1% formic acid, and 95% acetonitrile with 0.1% formic acid, and pooled. The combined volume of extracted peptides was then vacuum-concentrated to dryness. Peptides were then resuspended in 0.1% formic acid and desalted with a C18 ZipTip (MilliporeSigma) following manufacturer instructions. The peptides were eluted in 95% acetonitrile with 0.1% formic acid, vacuum-concentrated to dryness, and then resuspended in 20 µL of 20% acetonitrile with 0.1% formic acid.

Digested peptides were characterized by LC–MS/MS using a Thermo Scientific Fusion mass spectrometer with a Dionex Ultimate 3000 UHPLC system using an nLC column (200×75 mm) packed with Vydac 5 mm particles of 300 Å pore size (Hichrom Limited). The following solvents: 0.1% FA in water (solvent A) and 0.1% FA in acetonitrile (solvent B) were used for the LC method. After a 4.5 min equilibration of 20% solvent B at a flow rate of 1 µL/min, the flow rate was dropped to 0.3 µL/min over 0.5 min. The sample was then injected and the gradient run was as follows: solvent B at 20%–85% for 32 min, 85% for 2 min. Mass spectra were acquired in positive-ion mode. Full MS was done at a resolution of 60,000 [automatic gain control (AGC) target, 4×10^5; maximum ion trap (IT), 50 ms; range, 150–1800 m/z], and data-dependent and targeted MS/MS were both performed at a resolution of 15,000 [AGC target, 5×10^5; maximum IT, 500 ms; isolation window, 2.2] using higher-energy collisional dissociation (HCD) fragmentation. HCD collision energy was 18% with steps of 3% during LC–MS/MS measurements.

For data acquisition of the core peptide, a modified LC gradient was used. After the sample was injected, the gradient run was as follows: solvent B at 20–85% over 21 min, 85% for 1 min. All other parameters were the same as the method above. Only data-dependent MS/MS was performed. Samples were run in duplicate for integration of the abundance of each methylated species.

Data were processed and analyzed using Thermo Fisher Xcalibur 3.0.63 and MaxQuant v1.6.10.

4.7 | Crystallization

After size exclusion chromatography, protein complexes were dialyzed into 10 mM HEPES pH 8 and concentrated to 20 mg/mL. Crystal trays (Hampton Research) were set up using the hanging-drop method and three ratios of protein to well solution (1:1, 2:1, and 3:1). A modified screening of conditions for the wt complex was performed, where the pH of 240 mM sodium malonate and the percentage of PEG 3350 of the well solution were varied. The best conditions for SonM•SonA-L63D•SAH were 240 mM sodium malonate pH 5.5 with 12% PEG 3350 and 0.5 mM SAH. The best conditions for SonM•SonA-L63D•SAM were 240 mM sodium malonate pH 5.5 with 2% PEG 3350 and 1 mM SAM. The best conditions for SonM•SonA-L63D (apo) were 240 mM sodium malonate pH 5.5 with 8% PEG 3350. The best conditions for SonM•SonA-I65W (apo) were 240 mM sodium malonate pH 5.5 with 10% PEG 3350. Both SonM•SonA-I65W•SAH and SonM•SonA-I65W•SAM best crystallized in 240 mM sodium malonate pH 5.5 with 14% PEG 3350 and either 0.5 mM SAH or 1 mM SAH, respectively. All above variant co-crystals were cryoprotected in 240 mM sodium malonate pH 5.5, 20% PEG 3350, 20% glycerol, and the same concentration of cofactor where indicated. SonM•SonA-Y62A•SAH was co-crystallized in 240 mM sodium malonate pH 6, 12% PEG 3350, and 1 mM SAH and cryoprotected in 240 mM sodium malonate pH 6, 21% PEG 3350, 20% glycerol, and 1 mM SAH. SonM•SonA-Y62A•SAM was co-crystallized in 240 mM sodium malonate pH 5.5, 12% PEG 3350, and 1 mM SAH and cryoprotected in 240 mM sodium malonate pH 5.5, 21% PEG 3350, 20% glycerol, and 1 mM SAM. SonM•SonA-Y62A was also crystallized in absence of cofactor in 240 mM sodium malonate pH 5.5 and 22% PEG 3350 and cryoprotected in 240 mM sodium malonate pH 5.5, 27% PEG 3350 and 20% glycerol. After looping and transferring briefly into the cryoprotectant, crystals were flash frozen in liquid nitrogen and shipped to the synchrotron.

4.8 | X-ray data collection, structure resolution, and refinement

X-ray diffraction datasets were collected at 100 K using synchrotron radiation on the 23-IDB and 23-IDD beamlines at the Advanced Photon Source (APS, Argonne, IL). The X-ray diffraction data were integrated and scaled using the XDS package (Kabsch 2010). Several datasets presented unexpected complications. First, several crystals unexpectedly belonged to the P1 space group, while the wt and other mutant complexes would typically be processed in higher symmetry level space groups (e.g., P2$_1$ for 7LTE). For some data sets, despite collecting over 210°, this results in lower than desired but sufficient completeness. Second, while some of these datasets (i.e., SonM•SonA-I65W•SAH; SonM•SonA-L63D•SAH and SAM; SonM•SonA-Y62A•SAH) could be processed in P2$_1$ with unit cell parameters very close to 7LTE and the structures solved with this space group, this resulted in very poor maps and equally poor refinement statistics. Analysis with Xtriage (Zwart et al. 2005) revealed that these datasets likely suffer from pseudosymmetry and possibly twinning. We surmise that the heterogeneity of the species may have caused the 2$_1$ symmetry axis to only be partly present in the crystals. The above-mentioned datasets were subsequently re-processed in P1, and refined using REFMAC (Emsley et al. 2010) and twin refinement with parameters depicted in Table S2. This procedure resulted in largely improved refinement statistics and maps. While no correction can fully remediate such a data issue (and this is reflected in the refinement R factor statistics, for example), it allowed for the production of maps informative enough to build meaningful models, although their interpretation can be limited by the reduced electron density map quality. Generally, the structures were solved using molecular replacement using the wt SonM•SonA-2Me•SAH structure as a model (PDB: 7LTE) and the MOLREP software (Vagin and Teplyakov 2010). Model construction was done using Coot 0.9.8.1 (Emsley et al. 2010). Refinement was performed using REFMAC for all structures but SonM•SonA-L63D-SAM for which PHENIX was used (Adams et al. 2011) and produced better maps than REFMAC with or without twin refinement. All final refinement statistics are shown in Table S2. Sometimes, core peptides were modeled very partially based on the residual maps of the SonM active site. Unless otherwise noted, figures represent the molecules that are best supported by the electronic density maps. Polder maps were calculated using PHENIX (Liebschner et al. 2019). All structures were deposited to the Protein Data Bank.

4.9 | PDB sequence segment search

The RCSB Protein Data Bank (PDB) was searched using two Python scripts in succession. The first, primary structure searcher.py, was given a template sequence and list of sequence motifs and output a list of the PDB ID numbers for all unique crystal structures that included the motif(s) in their primary sequences.

The second script, secondary structure analyzer.py, was given the list of PDB IDs output by the first script.

The second script downloaded each of these PDB files, analyzed each protein's secondary structure, and returned a comma-delimited file that included the ID number, segment sequence matching the motif, and the secondary structure of each amino acid residue in that sequence. Structures were not included in the list if they contained amino acids in the sequence that were not resolved in the crystal structure or if they could not be loaded successfully into Rosetta because of incompatibility issues in the file.

For assays with SonM, we selected four sequences, two with α-helical secondary structure and two with β-sheet structure in their native structures from the PDB as well as when appended to the C-terminus of SonA, as predicted by PSIPRED and AlphaFold2.

AUTHOR CONTRIBUTIONS

ACKNOWLEDGMENTS

ORCID

Kathryn K. Crone https://orcid.org/0000-0001-9888-4710
Mikael H. Elias https://orcid.org/0000-0003-0406-7539
Michael F. Freeman https://orcid.org/0000-0002-0491-9618

REFERENCES

Adams PD, Afonine PV, Bunkóczi G, Chen VB, Echols N, Headd JJ, et al. The Phenix software for automated determination of macromolecular structures. Methods. 2011;55(1):94–106. https://doi.org/10.1016/j.ymeth.2011.07.005

Arnison PG, Bibb MJ, Bierbaum G, Bowers AA, Bugni TS, Bulaj G, et al. Ribosomally synthesized and post-translationally modified peptide natural products: overview and recommendations for a universal nomenclature. Nat Prod Rep. 2013;30(1):108–60. https://doi.org/10.1039/C2NP20085F

Borel JF, Feurer C. Effects of the new anti-lymphocytic peptide cyclosporin A in animals. Immunology. 1977;32:1017–25.

Burkhart BJ, Kakkar N, Hudson GA, van der Donk WA, Mitchell DA. Chimeric leader peptides for the generation of non-natural hybrid RiPP products. ACS Cent Sci. 2017;3(6):629–38. https://doi.org/10.1021/acscentsci.7b00141

Cai X, Zhao L, Bode HB. Engineering of specific single-module nonribosomal peptide synthetases of the RXP type for the production of defined peptides. ACS Synth Biol. 2023;12(1):203–12. https://doi.org/10.1021/acssynbio.2c00472

Chatterjee C, Patton GC, Cooper L, Paul M, van der Donk WA. Engineering dehydro amino acids and thioethers into peptides using lacticin 481 synthetase. Chem Biol. 2006;13(10):1109–17. https://doi.org/10.1016/j.chembiol.2006.08.015

Chatterjee J, Laufer B, Kessler H. Synthesis of *N*-methylated cyclic peptides. Nat Protoc. 2012;7(3):432–44. https://doi.org/10.1038/nprot.2011.450

Chatterjee J, Rechenmacher F, Kessler H. *N*-methylation of peptides and proteins: an important element for modulating biological functions. Angew Chem. 2013;52(1):254–69. https://doi.org/10.1002/anie.201205674

Chaudhury S, Lyskov S, Gray JJ. PyRosetta: a script-based interface for implementing molecular modeling algorithms using Rosetta. Bioinformatics. 2010;26(5):689–91. https://doi.org/10.1093/bioinformatics/btq007

Cheung WL, Pan SJ, Link AJ. Much of the microcin J25 leader peptide is dispensable. J Am Chem Soc. 2010;132(8):2514–5. https://doi.org/10.1021/ja910191u

Chou PY, Fasman GD. Prediction of protein conformation. Biochemistry. 1974;13(2):222–45. https://doi.org/10.1021/bi00699a002

Crone KK, Jomori T, Miller FS, Gralnick JA, Elias MH, Freeman MF. RiPP enzyme heterocomplex structure-guided discovery of a bacterial borosin α-*N*-methylated peptide natural product. RSC Chem Biol. 2023;4:804–16. https://doi.org/10.1039/d3cb00093a

Deane CD, Burkhart BJ, Saint-Vincent PMB, Tietz JI, Lin A, Mitchell DA. In vitro biosynthesis and substrate tolerance of the plantazolicin family of natural products. ACS Chem Biol. 2016;11(8):2232–43. https://doi.org/10.1021/acschembio.6b00369

DiCaprio AJ, Firouzbakht A, Hudson GA, Mitchell DA. Enzymatic reconstitution and biosynthetic investigation of the lasso peptide fusilassin. J Am Chem Soc. 2019;141(1):290–7. https://doi.org/10.1021/jacs.8b09928

Emsley P, Lohkamp B, Scott WG, Cowtan K. Features and development of Coot. Acta Crystallogr Sect D Biol Crystallogr. 2010;66(4):486–501. https://doi.org/10.1107/S0907444910007493

Franz L, Koehnke J. Leader peptide exchange to produce hybrid, new-to-nature ribosomal natural products. Chem Commun. 2021;57(52):6372–5.

Goto Y, Ito Y, Kato Y, Tsunoda S, Suga H. One-pot synthesis of azoline-containing peptides in a cell-free translation system integrated with a posttranslational cyclodehydratase. Chem Biol. 2014;21(6):766–74. https://doi.org/10.1016/j.chembiol.2014.04.008

Himes PM, Allen SE, Hwang S, Bowers AA. Production of sactipeptides in *Escherichia coli*: probing the substrate promiscuity of subtilosin A biosynthesis. ACS Chem Biol. 2016;11(6):1737–44. https://doi.org/10.1021/acschembio.6b00042

Imani AS, Lee AR, Vishwanathan N, de Waal F, Freeman MF. Diverse protein architectures and α-*N*-methylation patterns define split borosin RiPP biosynthetic gene clusters. ACS Chem Biol. 2022;17(4):908–17. https://doi.org/10.1021/acschembio.1c01002

Iwane Y, Kimura H, Katoh T, Suga H. Uniform affinity-tuning of *N*-methyl-aminoacyl-tRNAs to EF-Tu enhances their multiple incorporation. Nucleic Acids Res. 2021;49(19):10807–17. https://doi.org/10.1093/nar/gkab288

Jones DT. Protein secondary structure prediction based on position-specific scoring matrices. J Mol Biol. 1999;292(2):195–202. https://doi.org/10.1006/jmbi.1999.3091

Jumper J, Evans R, Pritzel A, Green T, Figurnov M, Ronneberger O, et al. Highly accurate protein structure prediction with AlphaFold. Nature. 2021;596(7873):583–9. https://doi.org/10.1038/s41586-021-03819-2

Kabsch W. XDS. Acta Crystallogr Sect D Biol Crystallogr. 2010;66(2):125–32. https://doi.org/10.1107/S0907444909047337

Kawakami T, Murakami H, Suga H. Messenger RNA-programmed incorporation of multiple *N*-methyl-amino acids into linear and cyclic peptides. Chem Biol. 2008;15(1):32–42. https://doi.org/10.1016/j.chembiol.2007.12.008

Kersten RD, Mydy LS, Fallon TR, De Waal F, Shafiq K, Wotring JW, et al. Gene-guided discovery and ribosomal biosynthesis of moroidin peptides. J Am Chem Soc. 2022;144(17):7686–92. https://doi.org/10.1021/jacs.2c00014

Khusainov R, Moll GN, Kuipers OP. Identification of distinct nisin leader peptide regions that determine interactions with the modification enzymes NisB and NisC. FEBS Open Bio. 2013;3:237–42. https://doi.org/10.1016/j.fob.2013.05.001

Kuipers OP, Bierbaum G, Ottenwälder B, Dodd HM, Horn N, Metzger J, et al. Protein engineering of lantibiotics. Antonie Van Leeuwenhoek. 1996;69(2):161–70. https://doi.org/10.1007/BF00399421

Lee AR, Carter RS, Imani AS, Dommaraju SR, Hudson GA, Mitchell DA, et al. Discovery of borosin catalytic strategies and function through bioinformatic profiling. ACS Chem Biol. 2024;19:1116–24. https://doi.org/10.1021/acschembio.4c00066

Levitt M. Conformational preferences of amino acids in globular proteins. Biochemistry. 1978;17(20):4277–85. https://doi.org/10.1021/bi00613a026

Li B, Sher D, Kelly L, Shi Y, Huang K, Knerr PJ, et al. Catalytic promiscuity in the biosynthesis of cyclic peptide secondary metabolites in planktonic marine cyanobacteria. Proc Natl Acad Sci. 2010;107(23):10430–5. https://doi.org/10.1073/pnas.0913677107

Li X, Wang N, Liu Y, Li W, Bai X, Liu P, et al. Backbone *N*-methylation of peptides: advances in synthesis and applications in pharmaceutical drug development. Bioorg Chem. 2023;141:106892. https://doi.org/10.1016/j.bioorg.2023.106892

Liebschner D, Afonine PV, Baker ML, Bunkóczi G, Chen VB, Croll TI, et al. Macromolecular structure determination using X-rays, neutrons and electrons: recent developments in Phenix. Acta Crystallogr Sect D Struct Biol. 2019;75(Pt 10):861–77. https://doi.org/10.1107/S2059798319011471

Mavaro A, Abts A, Bakkes PJ, Moll GN, Driessen AJM, Smits SHJ, et al. Substrate recognition and specificity of the NisB protein, the lantibiotic dehydratase involved in nisin biosynthesis. J Biol Chem. 2011;286(35):30552–60. https://doi.org/10.1074/jbc.M111.263210

Miller FS, Crone KK, Jensen MR, Shaw S, Harcombe WR, Elias MH, et al. Conformational rearrangements enable iterative backbone *N*-methylation in RiPP biosynthesis. Nat Commun. 2021;12(1):5355. https://doi.org/10.1038/s41467-021-25575-7

Montalbán-López M, Scott TA, Ramesh S, Rahman IR, van Heel AJ, Viel JH, et al. New developments in RiPP discovery, enzymology and engineering. Nat Prod Rep. 2021;38(1):130–239. https://doi.org/10.1039/D0NP00027B

Mydy LS, Hungerford J, Chigumba DN, Konwerski JR, Jantzi SC, Wang D, et al. An intramolecular macrocyclase in plant ribosomal peptide biosynthesis. Nat Chem Biol. 2024;20:530–40. https://doi.org/10.1038/s41589-024-01552-1

Quijano MR, Zach C, Miller FS, Lee AR, Imani AS, Künzler M, et al. Distinct autocatalytic α-*N*-methylating precursors expand the borosin RiPP family of peptide natural products. J Am Chem Soc. 2019;141(24):9637–44. https://doi.org/10.1021/jacs.9b03690

Ramm S, Krawczyk B, Mühlenweg A, Poch A, Mösker E, Süssmuth RD. A self-sacrificing *N*-methyltransferase is the precursor of the fungal natural product omphalotin. Angew Chem Int Ed. 2017;56(33):9994–7. https://doi.org/10.1002/anie.201703488

Reyna-González E, Schmid B, Petras D, Süssmuth RD, Dittmann E. Leader peptide-free in vitro reconstitution of microviridin biosynthesis enables design of synthetic protease-targeted libraries. Angew Chem Int Ed. 2016;55(32):9398–401. https://doi.org/10.1002/anie.201604345

Rink R, Kluskens LD, Kuipers A, Driessen AJM, Kuipers OP, Moll GN. NisC, the cyclase of the lantibiotic nisin, can catalyze cyclization of designed nonlantibiotic peptides. Biochemistry. 2007;46(45):13179–89. https://doi.org/10.1021/bi700106z

Sardar D, Lin Z, Schmidt EW. Modularity of RiPP enzymes enables designed synthesis of decorated peptides. Chem Biol. 2015a;22(7):907–16. https://doi.org/10.1016/j.chembiol.2015.06.014

Sardar D, Pierce E, McIntosh JA, Schmidt EW. Recognition sequences and substrate evolution in cyanobactin biosynthesis. ACS Synth Biol. 2015b;4(2):167–76. https://doi.org/10.1021/sb500019b

Sarkar S, Gu W, Schmidt EW. Applying promiscuous RiPP enzymes to peptide backbone *N*-methylation chemistry. ACS Chem Biol. 2022;17(8):2165–78. https://doi.org/10.1021/acschembio.2c00293

Scholtz JM, York EJ, Stewart JM, Baldwin RL. A neutral, water-soluble, alpha-helical peptide: the effect of ionic strength on the helix-coil equilibrium. J Am Chem Soc. 1991;113(13):5102–4. https://doi.org/10.1021/ja00013a079

Sciarretta KL, Boire A, Gordon DJ, Meredith SC. Spatial separation of β-sheet domains of β-amyloid: disruption of each β-sheet by *N*-methyl amino acids. Biochemistry. 2006;45(31):9485–95. https://doi.org/10.1021/bi0605585

Song H, Burton AJ, Shirran SL, Fahrig-Kamarauskaitė J, Kaspar H, Muir TW, et al. Engineering of a peptide α-*N*-methyltransferase to methylate non-proteinogenic amino acids. Angew Chem Int ed. 2021a;60(26):14319–23. https://doi.org/10.1002/anie.202100818

Song H, Fahrig-Kamarauskaitė J, Matabaro E, Kaspar H, Shirran SL, Zach C, et al. Substrate plasticity of a fungal peptide α-*N*-methyltransferase. ACS Chem Biol. 2020;15(7):1901–12. https://doi.org/10.1021/acschembio.0c00237

Song H, van der Velden NS, Shiran SL, Bleiziffer P, Zach C, Sieber R, et al. A molecular mechanism for the enzymatic methylation of nitrogen atoms within peptide bonds. Sci Adv. 2018;4(8):1–12. https://doi.org/10.1126/sciadv.aat2720

Song I, Kim Y, Yu J, Go SY, Lee HG, Song WJ, et al. Molecular mechanism underlying substrate recognition of the peptide macrocyclase PsnB. Nat Chem Biol. 2021b;17(11):1123–31. https://doi.org/10.1038/s41589-021-00855-x

Soto P, Griffin MA, Shea JE. New insights into the mechanism of Alzheimer amyloid-β fibrillogenesis inhibition by *N*-methylated peptides. Biophys J. 2007;93(9):3015–25. https://doi.org/10.1529/BIOPHYSJ.107.112086

Subtelny AO, Hartman MCT, Szostak JW. Ribosomal synthesis of *N*-methyl peptides. J Am Chem Soc. 2008;130(19):6131–6. https://doi.org/10.1021/ja710016v

Thokkadam A, Do T, Ran X, Brynildsen MP, Yang ZJ, Link AJ. High-throughput screen reveals the structure–activity relationship of the antimicrobial lasso peptide ubonodin. ACS Cent Sci. 2023;9(3):540–50. https://doi.org/10.1021/acscentsci.2c01487

Vagin A, Teplyakov A. Molecular replacement with MOLREP. Acta Crystallogr Sect D Biol Crystallogr. 2010;66(1):22–5. https://doi.org/10.1107/S0907444909042589

Vagstad AL. Engineering ribosomally synthesized and posttranslationally modified peptides as new antibiotics. Curr Opin Biotechnol. 2023;80:102891. https://doi.org/10.1016/j.copbio.2023.102891

van der Velden NS, Kälin N, Helf MJ, Piel J, Freeman MF, Künzler M. Autocatalytic backbone *N*-methylation in a family of ribosomal peptide natural products. Nat Chem Biol. 2017; 13(8):833–5. https://doi.org/10.1038/nchembio.2393

Weiz AR, Ishida K, Makower K, Ziemert N, Hertweck C, Dittmann E. Leader peptide and a membrane protein scaffold guide the biosynthesis of the tricyclic peptide microviridin. Chem Biol. 2011;18(11):1413–21. https://doi.org/10.1016/j.chembiol.2011.09.011

Yang X, Lennard KR, He C, Walker MC, Ball AT, Doigneaux C, et al. A lanthipeptide library used to identify a protein–protein interaction inhibitor. Nat Chem Biol. 2018;14(4):375–80. https://doi.org/10.1038/s41589-018-0008-5

Zhang L, Wang C, Chen K, Zhong W, Xu Y, Molnár I. Engineering the biosynthesis of fungal nonribosomal peptides. Nat Prod Rep. 2023;40(1):62–88. https://doi.org/10.1039/D2NP00036A

Zheng Y, Ongpipattanakul C, Nair SK. Bioconjugate platform for iterative backbone *N*-methylation of peptides. ACS Catal. 2022; 12(22):14006–14. https://doi.org/10.1021/acscatal.2c04681

Ziemert N, Ishida K, Liaimer A, Hertweck C, Dittmann E. Ribosomal synthesis of tricyclic depsipeptides in bloom-forming cyanobacteria. Angew Chem Int ed. 2008;47(40):7756–9. https://doi.org/10.1002/anie.200802730

Zwart PH, Grosse-Kunstleve RW, Adams PD. Xtriage and Fest: automatic assessment of X-ray data and substructure structure factor estimation. CCP4 Newsl. 2005;43:27–35.

SUPPORTING INFORMATION

Additional supporting information can be found online in the Supporting Information section at the end of this article.